INL/RPT-23-73230

Modeling DOE Standard Canister Configurations with Updated Surface Chemistry

June 2023

Alexander W. Abboud
Idaho National Laboratory

INL is a U.S. Department of Energy National Laboratory
operated by Battelle Energy Alliance, LLC

INL/RPT-23-73230

Modeling DOE Standard Canister Configurations with Updated Surface Chemistry

Alexander W. Abboud
Idaho National Laboratory

June 2023

Idaho National Laboratory
Idaho Falls, Idaho 83415

http://www.inl.gov

Prepared for the
U.S. Department of Energy
Office of Environmental Management
Under DOE Idaho Operations Office
Contract DE-AC07-05ID14517

SUMMARY

Road-ready and final disposition packaging configurations for the advanced test reactor (ATR) fuel currently specifies storage within helium backfilled DOE sealed standard canisters. The aluminum cladding of the ATR fuel contains an oxyhydroxide layer of boehmite/bayerite that generates hydrogen when subjected to irradiation. Understanding the effect of this hydrogen buildup over time to important for long term storage considerations. Previous modeling efforts have built a coupled CFD-chemical model to simulate the temperature gas phase concentrations within the DOE sealed standard canisters. These models have coupled the temperature conditions to both the gas phase radiolysis chemistry and the surface chemistry associated with the oxyhydroxide layer.

Continued experimental work has identified trends for aluminum surrogate samples with oxyhydroxide layers for tests done at higher dose rates. At low initial doses a fast generation rate of hydrogen occurs which starts to roll over to a lower generation rate as the total dose applied in increased. A previous study created a small-scale chemical model was built to replicate a mini-canister surrogate system at SRNL as well as for the smaller capsule tests performed at INL. The previous iteration of the model utilized step function for its G-values for the hydrogen generation over a 200-year period. This model makes an update to the surface chemistry to account for theorized surface chemistry reactions allowing for oxygen to remain bounded to the oxyhydroxide layer. As additional experiments continue, the kinetic fits may be adjusted to adapt to new data.

Three canister configurations are modeled – the base 18-inch, 15-foot DOR standard canister with 30 ATR fuel elements, an 18-inch, 10-foot DOE standard canister with 32 ATR fuel elements and a 24-inch, 10-foot DOE standard canister with 40 ATR fuel elements. In previous reports, the primary sensitivity of the canister conditions was identified as the decay heat of the fuel and the dried condition of the fuel. Only these parameters are studied in the report.

For the nominal case with dried fuel, the hydrogen generation is only about 2%, so it is even less than the flammability limit if it were exposed to oxygen. For the densely packed 18-inch case the total hydrogen concentration is only around 4% with the nominal decay heat. For the densely packed 24-inch case the total hydrogen concentration is only 2.5%, roughly 20% higher than the original packing design, and still under flammability conditions if exposed to oxygen.

ACKNOWLEDGEMENTS

This work was funded by the U.S. Department of Energy Environmental Management office. This work was performed by Battelle Energy Alliance, LLC, under DOE Idaho Operations Contract DE-AC07-05ID14517 and made use of the resources of the High Performance Computing Center at Idaho National Laboratory which is supported by the Office of Nuclear Energy of the U.S. DOE and the Nuclear Science User Facilities.

CONTENTS

SUMMARY iii
ACKNOWLEDGEMENTS iv
ACRONYMS vii
1. Introduction 1
2. Theory and Model Description 1
2.1 Thermal Fluid Model 1
2.2 Model Geometry 3
2.3 Sensitivity Conditions 4
2.4 Chemical Equations 6
3. Results and Discussion 9
3.1 CFD Model 9
3.2 Comparison with Previous Model 11
3.3 Chemical Modeling 11
4. Conclusions 13

FIGURES

Figure 1. Half domain used in simulations showing (a) fully loaded canister, (b) ATR element, (c) Type-1a basket, and (d) horizontal mesh slice. 3
Figure 2. The geometry layout for (a) 18-inch diameter and (b) 24-inch diameter canisters. The meshed geometry for (c) 18-inch diameter and (d) 24-inch diameter canisters. 4
Figure 3. Thermocouple measurements over 1 year in the INL CPP-603 facility for (a) one-hour intervals, (b) 12-hour and weekly intervals. 5
Figure 4. Fit to the hydrogen generation data of (a) coupon tests at INL and (b) mini canister test at SRNL, (c) coupon test with the $0-$ to $03-$ transition. Orange line shows the model, and blue dots show experimental data. 8
Figure 5. The steady state temperature for (a) 6-watt, (b) 18-watt and (c) 42-watt fuel elements in an 18-inch sealed canister base canister configuration, (d) 6-watt, (e) 18-watt and (f) 42-watt fuel elements in an 18-inch sealed canister densely packed canister configuration, and (g) 6-watt, (h) 18-watt and (i) 42-watt fuel elements in an 24-inch sealed canister densely packed canister configuration. 9
Figure 7. The transient average temperature profile for the (a) base configuration, (b) densely packed 18-inch canister and (c) densely packed 24-inch canister. 11

Figure 8. The (a) hydrogen gas generation of the three packing configurations here against the old model data and (b) the nitric acid concentrations 11
Figure 9. The (a) hydrogen concentration and (b) canister pressure for the base DOE canister configuration. 12
Figure 10. The (a) hydrogen concentration and (b) canister pressure for the densely-packed 18-inch DOE canister. 12
Figure 11. The (a) hydrogen concentration and (b) canister pressure for the base DOE canister configuration. 13

TABLES

Table 1. Physical properties of the components for a DOE Standard Sealed canister. 2
Table 2. Sensitivity parameters for this study. 5
Table 3. Decay heat values over time 10
Table 4. Summary of Results. 13

ACRONYMS

ATR	Advanced Test Reactor
ASNF	Aluminum-clad Spent Nuclear Fuel
CFD	Computational Fluid Dynamics
DOE	Department of Energy
INL	Idaho National Laboratory
MCO	Multi-Canister Overpack
MTHM	Metric tons of heavy metal
SNF	Spent Nuclear Fuel

Modeling DOE Standard Canister Configurations with Updated Surface Chemistry

1. Introduction

By the year 2035, there will be ~2500 MTHM of spent nuclear fuel (SNF) that will require geologic repository disposal that is managed by DOE. Approximately 400 Metric tons of heavy metal (MHTM) of this is currently not packaged (Lacroix et al., 2017). Previous studies in support of geologic disposal divided the DOE SNF inventory into 34 groups based on fuel matrix, cladding, cladding condition, and enrichment (Lacroix et al., 2017). The six aluminum clad fuel types are of interest as aluminum is significantly less corrosion resistant than stainless steel and zircaloy clad fuel. The aluminum cladding develops a corrosion layer that generates hydrogen from radiolysis, and can also contain bound, both physiosorbed and chemisorbed, water.

Over 30% of the volume of DOE stored fuel is aluminum clad. One source of the aluminum spent nuclear fuel (ASNF) that will continue to be produced and needs to be stored is the advanced test reactor (ATR) fuel at the Idaho National Laboratory (INL). The disposition path for this ASNF is to be loaded into road-ready DOE sealed standard canisters backfilled with helium for transportation and eventual long-term storage. This report is an iteration of the previous modeling efforts that were based on some of the early experimental data available. Follow up tests have been completed which show the roll-over effect of hydrogen generation at high doses (Horne et al., 2022; Verst, 2022), though may be inconclusive on if a true equilibrium is reached. The updated chemical model matches the experimental data that is available. The previous modeling efforts that utilized this G-value data showed that pressure gains, even with undried fuel are well under physical limitations with the dose rates for ATR fuel in sealed DOE canisters (Abboud 2021; Abboud 2022).

This study modifies the chemical model from the previous version that utilized a step-change in the G-value. The new chemistry model assumes that the water adsorbed in the oxyhydroxide matrix undergoes basic water radiolysis reactions, and that the aluminum oxyhydroxide breakdown into a series of reactions involving stable O^- and O_3^- groups. Conrad and Horne, 2023 & Conrad et al., 2022 present an overview of the literature for these mechanisms that involve the formation of an electron and hole pair (e^-, h^+) form in the solid from ionization and excitation. The literature exhibits several similar sets of mechanism by which result H atoms can combine to release H_2 that are adapted here in combination with equations consistent with hydrogen in water radiolysis (Milosavljevic et al, 2003; Thomas 2005; Buxton et al., 1998; Le Caer 2011).

2. Theory and Model Description

2.1 Thermal Fluid Model

The commercial multiphysics modeling platform STAR-CCM+ is used for modeling the canister (Siemens, 2022). The numerical solver implemented here is a finite-volume approach with second-order implicit time stepping and a second-order discretization scheme. The segregated flow solver for the Navier-Stokes equations is used, which is applicable to constant density or mildly compressible flows, with a predictor-corrector approach that couples the momentum and continuity equations. A collocated variable arrangement with a Rhie-Chow scheme for pressure-velocity coupling is implemented in a SIMPLE-type algorithm (Siemens,

2022). In the canister-scale models, the Reynolds is low enough such that laminar flow is assumed. The momentum equation is then given by

$$\frac{\partial(\rho \mathbf{v})}{\partial t} + \nabla \cdot (\rho \mathbf{v} \otimes \mathbf{v}) = -\nabla \cdot (p\mathbf{I}) + \nabla \cdot \mathbf{T} + \mathbf{f}_b \quad (1)$$

Where $\mathbf{v}$ is the velocity vector, $\mathbf{T}$, is the stress tensor, and ρ is the density. The $\boldsymbol{f}_b$ term is the body force, solely occurring due to the buoyancy driven flow in this case. The viscous stress tensor is

$$\mathbf{T} = \mu(\nabla \mathbf{v} + (\nabla \mathbf{v})^T) - \frac{2}{3}\mu(\nabla \cdot \mathbf{v})\mathbf{I} \quad (2)$$

Where μ is the gas viscosity. The mass conservation is expressed through the continuity equation

$$\frac{\partial \rho}{\partial t} + \nabla \cdot (\rho \mathbf{v}) = 0 \quad (3)$$

The conservation of energy gives an equation in terms of the total energy, E, as

$$\frac{\partial(\rho E)}{\partial t} + \nabla \cdot (\rho E \mathbf{v}) = \mathbf{f}_b \cdot \mathbf{v} + \nabla \cdot (\mathbf{v} \cdot \boldsymbol{\sigma}) - \nabla \cdot q + S_E \quad (4)$$

Where in the solid phases, the terms with $\mathbf{v}$ are equal to 0, q is the conductive heat flux, the energy source term S_E is due to the chemical reactions in the fluid phase and is from the specified heat source for the fuel plates in that solid region. The implicit solver in Star-CCM+ can typically adapt up to a Courant-Friedrichs-Lewy (CFL) condition of nearly 50. The properties for the materials used for each of the solid regions are shown in Table 1, it is assumed maximum temperatures are low enough to use constant thermal properties for solids.

Table 1. Physical properties of the components for a DOE Standard Sealed canister.

Material	Density [kg/m^3]	Thermal Conductivity [W/m K]	Heat Capacity [J/kg K]	Emissivity [-]
Al-6061 (siding/back plates) (Polkinghorne, 1991)	2702	167	896	0.82
Stainless Steel 304 (Incropera et al., 2007)	7900	14.9	477	0.46
Stainless Steel 316 (Incropera et al., 2007)	8238	13.4	468	0.46

ATR Fuel Plates (Illum, 1996)	3680	42.6	614	0.82 (assumed)

2.2 Model Geometry

For a DOE standard canister loaded with ATR spent fuel, the loading configuration is described in Kim et. al., with the basket configuration described in DOE/SNF/REP-90 and minor modifications for tolerance included in DOE/REP/DSN-19. The base loaded configuration uses the 15 foot long, 18-inch diameter configuration of the DOE standard canister constructed of stainless steel 316. Inside this are 3 Type 1a baskets, previously assumed to be made of stainless steel 304.

The fully loaded canister configuration used in the previous CFD model is shown in Figure 1a (Abboud and Huang 2019a), with the ATR fuel CAD shown in Figure 1b, and the Type 1a basket is shown in Figure 1c. Figure 1d shows a horizontal slice of the meshed domain used in the CFD simulations. The red denotes the fuel plates, the blue denotes the free volume of gas, the light grey shows the aluminum side plates, the medium grey shows the basket, and the outer dark grey shows the canister.

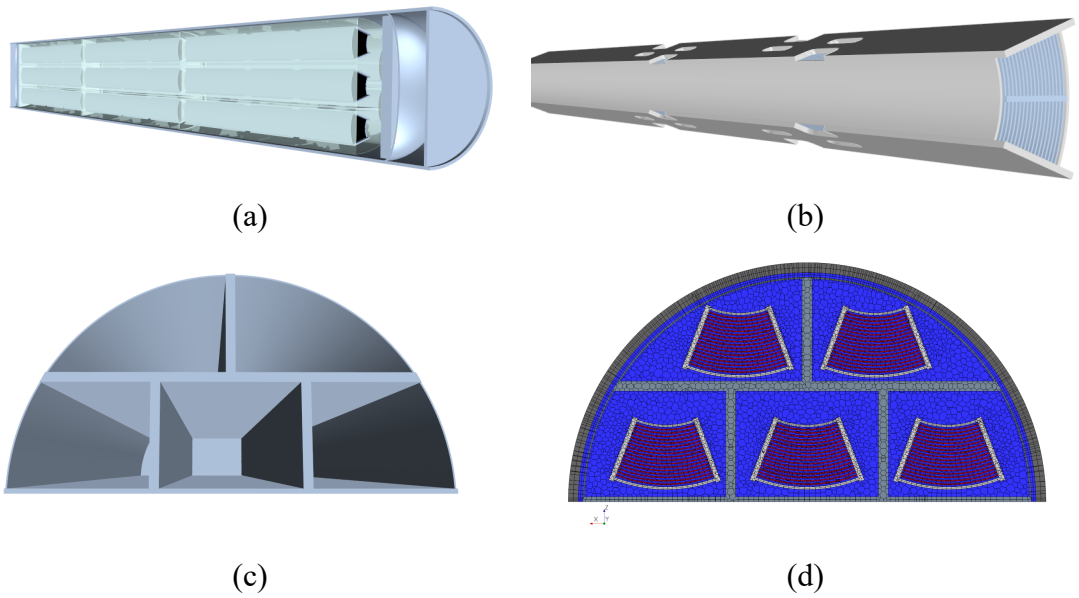

(a) (b) (c) (d)

Figure 1. Half domain used in simulations showing (a) fully loaded canister, (b) ATR element, (c) Type-1a basket, and (d) horizontal mesh slice.

Two additional model geometries were considered with denser packing configurations. The first of these is modified version of packing in an 18-inch diameter, 10-foot standard canister, but utilizing the ATR-4 buckets rather than the Type 1a baskets used previously. This increases the number of fuel elements per height from 10 to 16, for 32 total fuel elements. The second is packing in a 24-inch diameter, 10-foot standard canister, which also uses the ATR-4 buckets in a star-like configuration (Orano, 2019). This increases the fuel elements per height level up to 20, for 40 total fuel elements. Both configurations have a 2-inch spacer between the basket levels that is the diameter of the canister, as well as borated stainless-steel dividers between the buckets (shown in yellow). A diagram of these two configurations is shown in Figure 2a and Figure 2b, for the 18-inch and 24-inch diameter canisters, respectively. A meshed horizontal slice of the canister to show the packing is shown in Figure 2c and 2d for the 18-inch and 24-

inch diameter canisters, respectively. The maximum limits for these new canister configurations were estimated in Peterson 2023, and Abboud 2023.

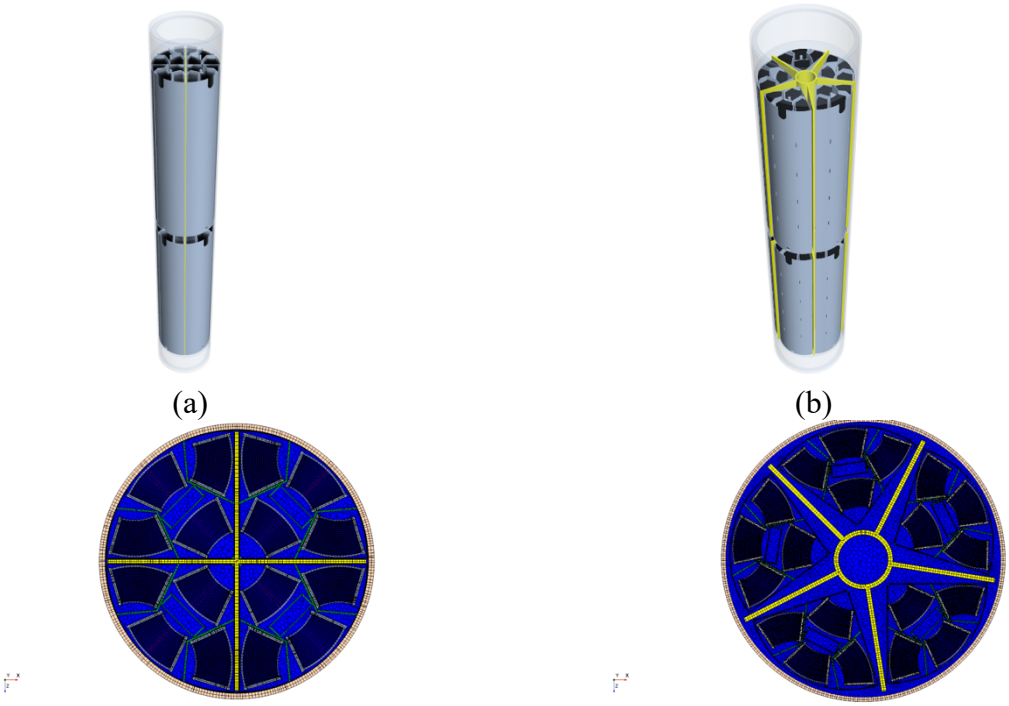

Figure 2. The geometry layout for (a) 18-inch diameter and (b) 24-inch diameter canisters. The meshed geometry for (c) 18-inch diameter and (d) 24-inch diameter canisters.

2.3 Sensitivity Conditions

The main parameters considered are the fuel decay heat, the aluminum oxyhydroxide layer thickness, and the drying condition of the fuel. Film oxyhydroxide layer thickness for a similar ASNF, from the University of Missouri research reactor (MURR) stored over a long duration in wet storage, were measured to be 5-10 μm, and measurements from the Mark-16B fuel from the SRS Production Reactors were measured to be 5-15 μm (Olson et al., 2019). The boehmite film on the ATR fuel is specified to be 2-6 μm by the manufacturer before reactor operation, and 1-4 μm was observed on measurements of end box samples in dry storage (Winston et al., 2020). A previous analysis of the fuel inventory list from Mortensen, 2016 to be moved into IFSF resulted in an average decay heat of 18 watts, with a standard deviation 12 watts. One standard deviation below was set as the lower bounds, and two standard deviations above was set as the upper bounds due to the large tail end of the distribution. The conditions outlined in Lundberg, 1992 and used in Wertsching 2007 at 34 μm and 22 μm as conservative estimates. While an estimate of the maximum pressure in a canister is very dependent on the thickness of this oxyhydroxide layer, the previous modeling reports showed nearly negligible dependence, so 5 μm is used here (Abboud 2021; Abboud 2023).

The initial pressure criterion for the DOE Standard Canisters, was defined as 345 kPa (g) (Morton, 1999). This design pressure was based off a maximum normal operating pressure (MNOP) of 150 kPa (g) anticipated at a proposed geologic repository (Abashian, 1998). Since then, finite element analysis modeling, and updated engineering calculations according to applicable codes and standards, have been performed that determined the actual structural pressure limit of the DOE Standard Canister was upwards

of 3,447 kPa (Snow 2019). While the design specification for the DOE Standard Canister does not address flammable or explosive gas mixture criteria, Section 4.3.11 of the Waste Acceptance System Requirements Document (US DOE, 2008) excludes flammable DOE Standard Canisters from disposition in a Civilian Radioactive Waste Management System. The lower flammability limit (LFL) of hydrogen in the presence of oxygen is 4% by volume (Zabetakis, 1965). However, with no oxygen in the gas phase, ignition of hydrogen will not occur. These two criteria – a pressure under 3,447 kPa and no oxygen dictate safe storage of SNF in DOE canisters.

As with the prior reports, an assumption is made that yearly temperatures for a 50-year storage scenario would mimic the conditions seen in the IFSF facility (Abboud and Huang, 2019b). Ambient temperatures for the INL INTEC CPP-603 facility are described in Christensen (2003a, b). A plot of the ambient temperature conditions measured when the facility had working thermocouples in 2011 is shown in Figure 3a, with 9 thermocouples recording once an hour over a year long period. The data in Figure 3b shows weeklong averages. The ambient temperature within the facility itself has a very small variation within it compared to the exterior climate due to the large amount of mass of spent fuel stored within it. The largest temperature difference in a 12-hour span is only 1.5° C, and largest temperature difference in a week-long span is 4.4° C. This justifies the large timesteps used for the CFD model for the thermal history. Table 2 includes the parameter ranges used in the study for decay heat and G-values based on the dried state of the fuel.

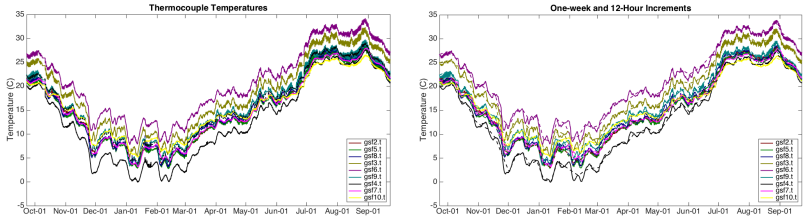

(a) (b)

Figure 3. Thermocouple measurements over 1 year in the INL CPP-603 facility for (a) one-hour intervals, (b) 12-hour and weekly intervals.

Table 2. Sensitivity parameters for this study.

Parameter	Lower Bound	Base Case	Upper Bound
G-value based on dryness [J/mol]	9.35×10^{-10} [dry]		4.91×10^{-10} [undried]
Decay Heat [W]	6	18	42

In ECAR 2906, MicroShield 9.01 was used to calculate the on-contact and 1-meter dosage rates for ATR fuel assemblies (Stewart 2012). Based on the decay heat for a given fuel assembly, the on-contact dosage rate can be estimated as

$$\dot{d} = 3.78 \times 10^{-3} Q, \tag{5}$$

in units of Gy/s, with Q as the decay heat rate given in Watts by

$$Q = Q_0 \exp\left(-0.023\, t_{year}\right) = Q_0 \exp\left(-7.2883 \times 10^{-10}\, t_{sec}\right) \tag{6}$$

2.4 Chemical Equations

The chemical reactions considered are one-step reactions, which are taken from the full chemical reaction mechanism earlier reported by Wittman & Hanson, 2015. This full mechanism contains 115 total reactions involving 40 chemical species. Wittman and Hanson developed this model was developed from literature for a full set of chemical reactions using prior experimental collection of radiolysis data (Bulearca et al., 2010, Atkinson et al., 2004; Arkhipov et al., 2007), and was used in the latest model of the DOE sealed standard canister with surface chemistry and in the unsealed canister modeling (Abboud 2023). Due to the nature of the long time-period of interest of this study, it would be infeasible to fully resolve all 40 chemical species and 115 total reactions within the canister due to the computational cost of multiphysics CFD models. The model utilizes Cantera for solution of the chemical reactions (Goodwin, 2017). The source term of chemical species is

$$\frac{d[A_i]}{dt} = \dot{d}\sum G_i w_g [A_g] + \sum k_{ir} \prod [A_{jr}]^{o_{jr}} \tag{7}$$

Where $\dot{d}$ is the dose rate, G_i is the G-value for the radiolytic decomposition, w_g is the molecular weight, k_{ir} is the reaction rate, and O_{jr} is the reaction order for species j. The transport equations for the species mass fractions, Y_i, are solved for N-1 species as

$$\frac{\partial \rho Y_i}{\partial t} + \nabla \cdot (\rho v Y_i) = \nabla \cdot \left(J_i + \frac{\mu_t}{\sigma_t} \nabla Y_i \right) + S_{Y_i} \tag{8}$$

The source term here, S_{Y_i}, is reformulated from equation 7 to be in terms of the mass fractions rather than concentration. The basic diffusion is defined as

$$J_i = \rho D_{i,m} \nabla Y_i \tag{9}$$

Where $D_{i,m}$ is the binary diffusion coefficient. The general reaction term is defined as

$$k_{ir} = k_{ir}^0 T^{x_r} \exp\left(-\frac{E_a}{RT}\right) \tag{10}$$

Based on the work completed by associated tasks for storage of aluminum-clad spent nuclear fuel, the surface chemistry associated with the aluminum cladding was added into the model to be coupled with the Wittman and Hanson gas phase model. This is done through work outlined for the radiolytic yield of the aluminum hydroxide (Zalupski 2018), the general surface corrosion (Lister 2018), and prior kinetic expressions for aluminum corrosion. While the surface chemistry built in Cantera is intended for catalytic reactions, it is utilized in this model as it allows for all parts of the metal to be reactive even if not at the surface. This estimate provides a conservative approximation which can be used as an upper bound. In creating the surface, one can calculate the number of moles of AlOOH present based on the plate thickness, and surface area of the plates

$$n_{AlOOH} = \frac{A_{fuel} th_{AlOOH} \rho_{AlOOH}}{MW_{AlOOH}} \tag{11}$$

The ratio of moles of oxide to moles of aluminum alloy is assumed proportional to the film thickness and the plate thickness

$$\theta_{AlOOH} = \frac{th_{AlOOH}}{th_{plate}/2} \tag{12}$$

While this may underestimate the total aluminum present to have a single surface, it is not that reactive at low temperatures. The calculation of the site density with this assumption is then

$$\rho_s = \frac{n_{AlOOH}}{X_{AlOOH} A_{fuel}} \tag{13}$$

The moles present for reaction is then

$$[\mathrm{AlOOH}] = \theta_{AlOOH} \rho_s \tag{14}$$

In the original version of the surface chemistry the H radical was assumed to directly evolve from the breakdown of boehmite (or another oxyhydroxide) as

$$2\ \mathrm{AlOOH(S)} \xrightarrow{\gamma} 2\ \mathrm{AlOO(S)} + 2\ \mathrm{H}\cdot \tag{15}$$

In this new surface chemistry model, this reaction has been removed. The following reactions are added to the model to account for the path of the oxyhydroxide to a stable O^- form. The g-value is just applied to the first reaction, other reactions are fit in python. The reactions also include intermediate breakdown of adsorbed water through radiolysis as a source of hydrogen.

$$\mathrm{Al\cdots OH} \xrightarrow{\gamma} \mathrm{h^+} + \mathrm{Al\cdots OH^-} \tag{16}$$
$$\mathrm{Al\cdots OH^-} \rightarrow \mathrm{Al\cdots O^{\cdot -}} + \mathrm{H^{\cdot}} \tag{17}$$
$$\mathrm{Al\cdots OH_2} + \mathrm{h^+} \rightarrow \mathrm{Al\cdots OH} + \mathrm{H^+} \tag{18}$$
$$\mathrm{H_2O} \xrightarrow{\gamma} \mathrm{e^-, H, H_2, OH, H_2O_2, H^+, H_2O^*} \tag{19}$$
$$\mathrm{H_2O^*} \rightarrow \mathrm{H_2} + \mathrm{O} \tag{20}$$

While there is evidence that additional reactions occur as listed below, converting the O^- to an O_3^- form characterized with electron paramagnetic resonance (Kaddissy et al, 2017; Kaddissy et al, 2017), fitting kinetic rates to the experimental data repeatedly resulted in a shift to the equilibrium such that no true roll-over would occur, and the hydrogen generation would ramp up over time. It's possible this pathway could refit, and that the optimization algorithm being used was overfitting these reactions, and this could be revisited in the future.

$$\mathrm{Al\cdots O^{\cdot -}} + \mathrm{Al\cdots O^{\cdot -}} \rightarrow \mathrm{Al\cdots O_2^{\cdot 2-} \cdots Al} \tag{21}$$
$$\mathrm{Al\cdots O_2^{2-} \cdots Al} + \mathrm{h^+} \rightarrow \mathrm{Al\cdots O_2^{\cdot -} \cdots Al} \tag{22}$$
$$\mathrm{Al\cdots O_2^{\cdot -} \cdots Al} + \mathrm{h^+} \rightarrow \mathrm{Al\cdots O_2 \cdots Al} \tag{23}$$
$$\mathrm{Al\cdots O_2 \cdots Al} + \mathrm{Al\cdots O^{\cdot -}} \rightarrow \mathrm{Al\cdots O_3^{\cdot -} \cdots Al} \tag{24}$$

The kinetic parameters for these new equations were fit utilizing the scipy optimize library with the "Nelder-Mead" method, where the optimization function was the minimization of the error between the chemical model and the experimental results. This error was normalized to minimize the hydrogen prediction as a function of the total dose of the tests. However, this often caused an overfit towards the end of the data for the coupons, so manual adjustments were made to decrease some of the kinetic fits to the data to prevent this overfitting. The kinetics rates for the new surface chemistry in Cantera are included in Appendix A. Figure 4a shows the figure to the Al6061 coupons at INL, Figure 4b shows the fit to the mini-canister tests at SRNL, and Figure 4c shows the results of adding the O^- to O_3^- transition reactions. As mentioned, these reactions could still occur, but relying on scipy fitting algorithm to minimize error resulted in an issue with the generation rates at high dose.

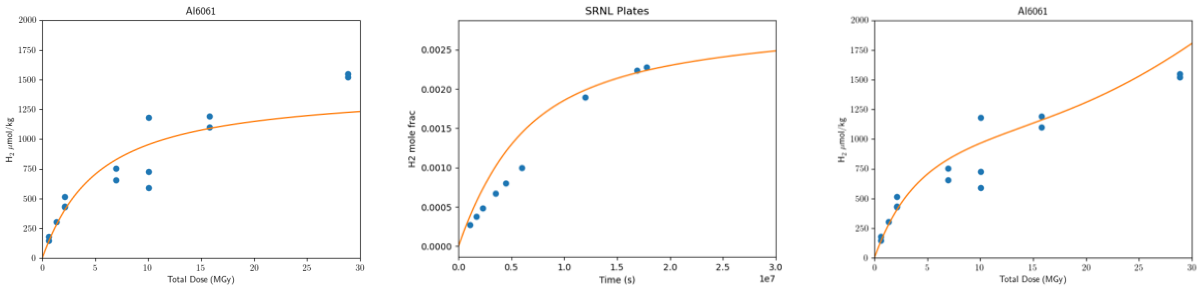

(a) (b) (c)

Figure 4. Fit to the hydrogen generation data of (a) coupon tests at INL and (b) mini canister test at SRNL, (c) coupon test with the O^- to O_3^- transition. Orange line shows the model, and blue dots show experimental data.

The 40+ reactions from (Wren and Ball, 2001) for water radiolysis are also used with the same overall kinetic rates, with a constant multiplier to the kinetic rates accounting for expressing the volumetric reaction as a surface reaction. The one exception is the reaction for $e^-(S) + H^+(S) \rightarrow H(S)$, which has its reaction rate increased by a factor of 10, otherwise all H on the surface remains stuck as H+ and rarely enters the gas phase. Lastly, the general corrosion of aluminum based on an older study (Hilton, 2000) in the event that the oxyhydroxide layer was consumed was also considered. This reaction was adapted from aluminum in water rather than humid air, and should therefore be conservative to include the reaction of

$$Al(S) + 1.5\ H_2O \rightarrow 0.5\ Al_2O_3(S) + 1.5H_2(g) \quad (17)$$

Nevertheless, it should be noted that this last equation has the most minimal effect in previous modeling. A rough estimation at an average surface temperature of 50 °C, the total aluminum corrosion would only be 1.2 grams after 50 years, or 58 grams after 50 years at 200 °C surface temperature.

3. Results and Discussion

3.1 CFD Model

A CFD model for the new canister configurations was constructed and ran at the initialization temperature. Figure 5a-c shows the temperature profile for the cases of the 18-inch canister with the base packing that was previously modeled for reference for the low, nominal and upper decay heat of the fuel. Figure 5d-f shows the temperature profile for the cases of the 18-inch canister with the 4 ATR-4 buckets configuration. Figure 5g-i shows the temperature profile for the cases of the 24-inch canister with the 5 ATR-4 buckets configuration. The plotted temperature profiles are at the start of the transient time period of the IFSF temperature plot, such that this is not the peak exterior temperatures. The peak temperatures in the more densely pack canister increased across all cases of decay heat. Visually, the contours of the densely packed canisters show they are hotter throughout the entire configuration.

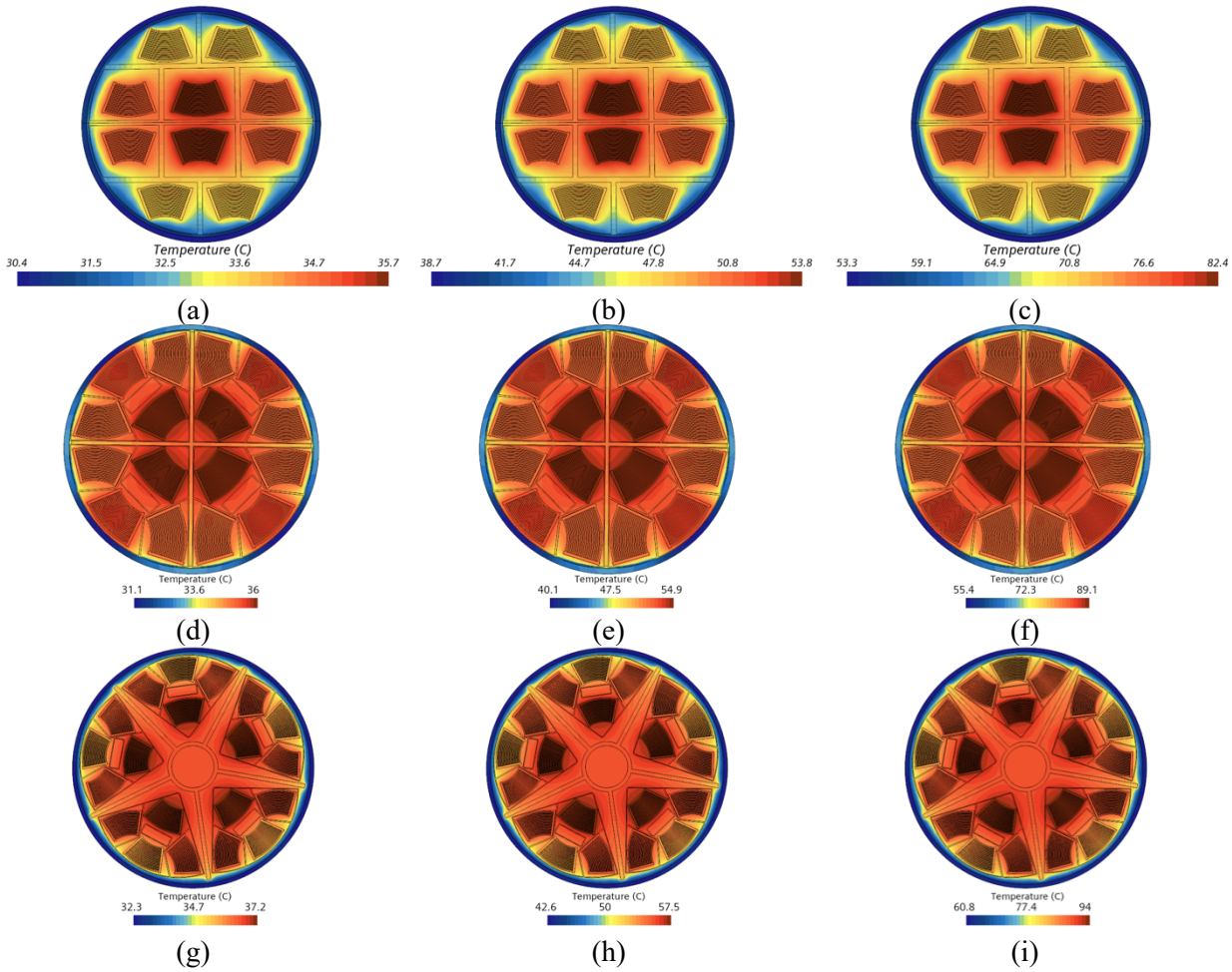

Figure 5. The steady state temperature for (a) 6-watt, (b) 18-watt and (c) 42-watt fuel elements in an 18-inch sealed canister base canister configuration, (d) 6-watt, (e) 18-watt and (f) 42-watt fuel elements in an 18-inch sealed canister densely packed canister configuration, and (g) 6-watt, (h) 18-watt and (i) 42-watt fuel elements in an 24-inch sealed canister densely packed canister configuration.

The histograms for the gas temperature at the start of the simulations are shown in Figure 6. These highlight the differences in the gas temperature distribution across the configurations. Figure 6a shows the original cases, with a histogram fairly close to a normal distribution. Figure 6b shows the densely packed

18-inch case, here there is a lot less temperature gradients within the canister and most of the gas is at a much hotter temperature, even though peak temperatures are only slightly higher. Figure 6c shows the histogram for the densely packed 24-inch canister, as with the other densely packed configuration this shifts temperatures to be significantly higher throughout the canister rather than being closer to the normal distribution of the base case. These higher temperatures will have an impact on the pressure buildup as hydrogen in generated in the systems.

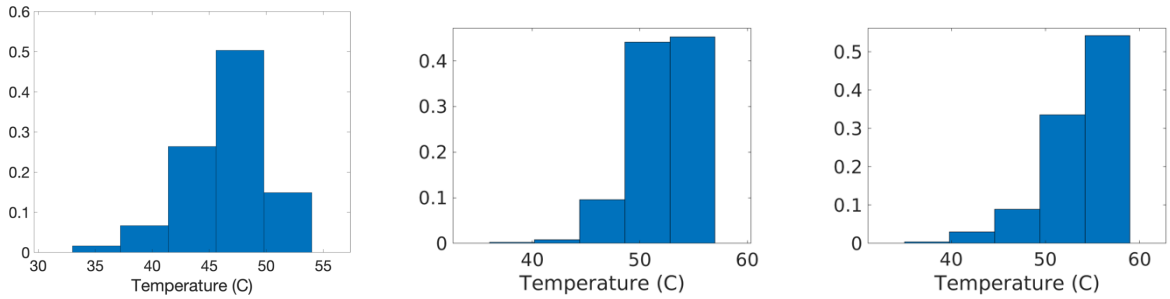

(a) (b) (c)

Figure 6. The steady state histograms for gas temperature for (a) base configuration, (b) densely packed 18-inch canister and (c) densely packed 24-inch canister.

To adapt to the longer timeframe, the thermal-CFD model has been extended for the additional time frame, out to 200 years. After 100 years most of the cases are practically at room temperature as the decay heat has decreased by a factor of 10. A step of 10 years out to 200 years was created for each case, this decreases the decay heat by a factor of 100. At this point any additional thermal modeling is proven unnecessary as the canisters are effectively bound by the exterior ambient temperature. Table 3 shows the decay heat for the fuels. Figure 7 shows the average gas temperature for the canister for the three packing configuration cases, which will still oscillate over timeout at 200 years, this is solely due to the oscillation of the building temperature as the ambient exterior temperature from Figure 3, and effectively all three cases have no thermal gradients and are at room temperature. The average temperature of the high decay heat case is increased by about 20C over the base configuration due to the closer proximity of the fuel.

Table 3. Decay heat values over time

Time [yr]	Low Decay Heat	Nominal Decay Heat	Upper Decay Heat
0	6	18	42
10	4.77	14.3	33.4
50	1.9	5.71	13.3
100	0.6	1.8	4.21
150	0.19	0.57	1.33
200	0.06	0.18	0.42

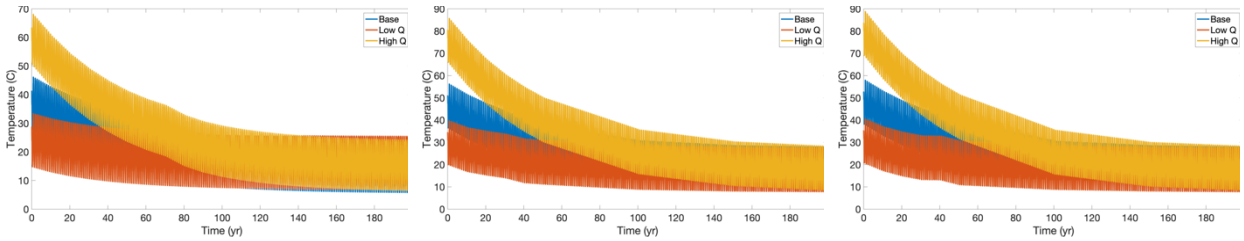

(a) (b) (c)

Figure 7. The transient average temperature profile for the (a) base configuration, (b) densely packed 18-inch canister and (c) densely packed 24-inch canister.

3.2 Comparison with Previous Model

A plot of the comparison of the models here against the model developed previously (Abboud, 2022) are shown in Figure 8. Figure 8a shows the standard DOE packing configuration with the model developed here, the base configuration is included for a direct comparison, and the two densely packed 18-inch and 24-inch canisters are included as well. In this new model, the roll-over effect occurs more quickly in the time frame, which causes the final model hydrogen concentration to be decreased by about a factor of 2. The densely packed 18-inch and 24-inch canister are of course higher than the base case due to the higher surface area to volume ratio. In this new model, the correction shows that the densely packed 18-inch canister only reaches about 4% mole percent hydrogen after a 200-year span, about the same value as the old model in the less dense configuration. Figure 8b shows the nitric acid generation under the assumption of 1% air ingress/residual air. The new model has a slightly lower generation rate, about 15% after the 200 yearlong span, mostly due to the lack of thermal dehydration in the new model maintaining a slightly lower total number of oxygen atoms form water vapor to scavenge for the nitic acid reactions.

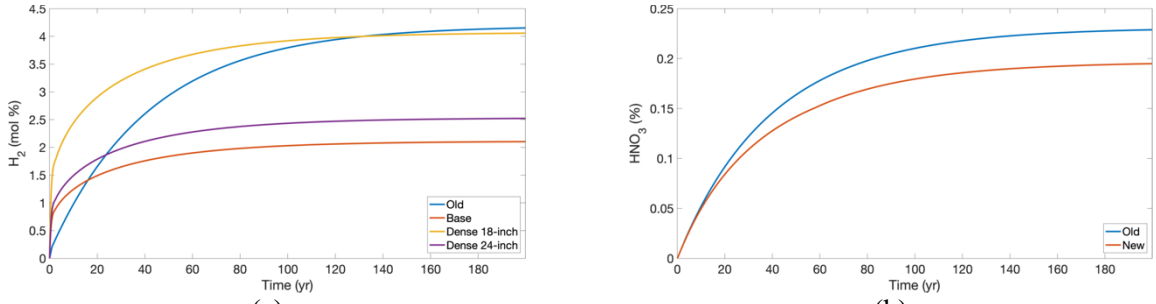

(a) (b)

Figure 8. The (a) hydrogen gas generation of the three packing configurations here against the old model data and (b) the nitric acid concentrations

3.3 Chemical Modeling

As discussed in previous reports, the initial decay heat of the fuel is by far the most important parameter which affects the hydrogen generation in the system. The results for the variation of the decay heat for the original canister configuration for the new model are in Figure 9. The hydrogen concentration is shown in Figure 9a. The low decay heat case shows a decrease of the hydrogen generation to near 1.5%, with an equilibrium effectively being reached after the first couple decades, the high decay heat case rollover but continues to show additional generation for long periods of time up to a concentration of 6%, but it should be noted this is far lower than the previous model at 9%. The pressure change is shown in Figure 9b. All cases show initial spikes in pressure, but the high decay heat case shows a significant

drop as the temperature decreases more significantly over time, the maximum pressure across the cases remains rather minimal changes slightly over 1 atm.

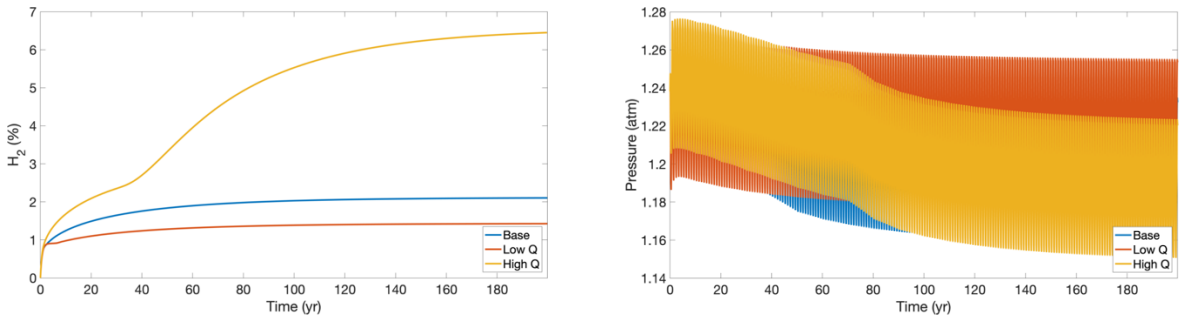

(a) (b)

Figure 9. The (a) hydrogen concentration and (b) canister pressure for the base DOE canister configuration.

The results for the variation of the decay heat for the densely packed 18-inch canister configuration are shown in Figure 10. The hydrogen concentration is shown in Figure 10a. The low decay heat case shows a decrease of the hydrogen generation to near 2.5%, with an equilibrium effectively being reached after the first couple decades. The upper decay heat case continues to produce hydrogen for long after the other two eventually reaching about 11% for its hydrogen concentration. The pressure change is shown in Figure 10b. All cases show initial spikes in pressure, but the high decay heat case shows a significant drop as the temperature decreases more significantly over time, the maximum pressure across the cases remains rather minimal changes slightly over 1 atm. Due to the high temperature of the more densely packed canister, the decline in the pressure of the high decay heat case is far steep over time than the original packing configuration.

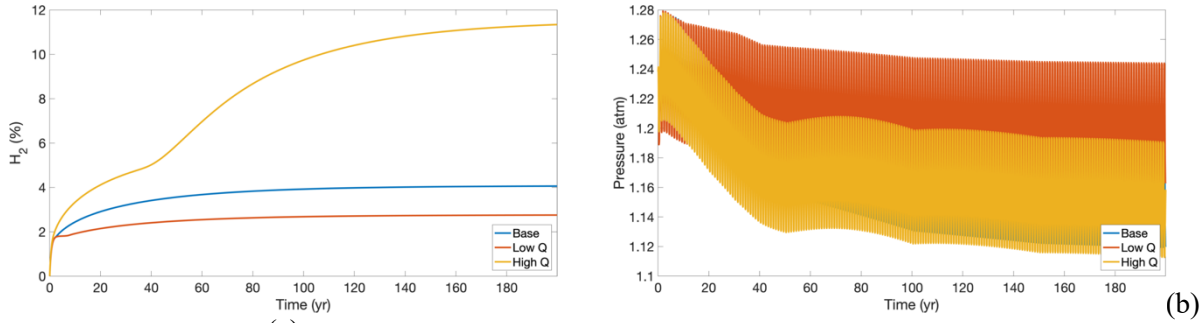

(a) (b)

Figure 10. The (a) hydrogen concentration and (b) canister pressure for the densely-packed 18-inch DOE canister.

The results for the densely packed 24-inch DOE canister as a function of the decay heat are shown in Figure 11. The hydrogen concentration is shown in Figure 11a. The low decay heat case shows a decrease of the hydrogen generation to near 1.7%, and as with other low decay heat cases reaches it equilibrium fairly quickly. The upper decay heat case reaches about 8% over the 200 year timeframe. The pressure change is shown in Figure 11b. As with the other densely packed case, due to the higher average temperature this experiences a sharper decline in pressure over time as the canister temperature eventually reaches room temperature.

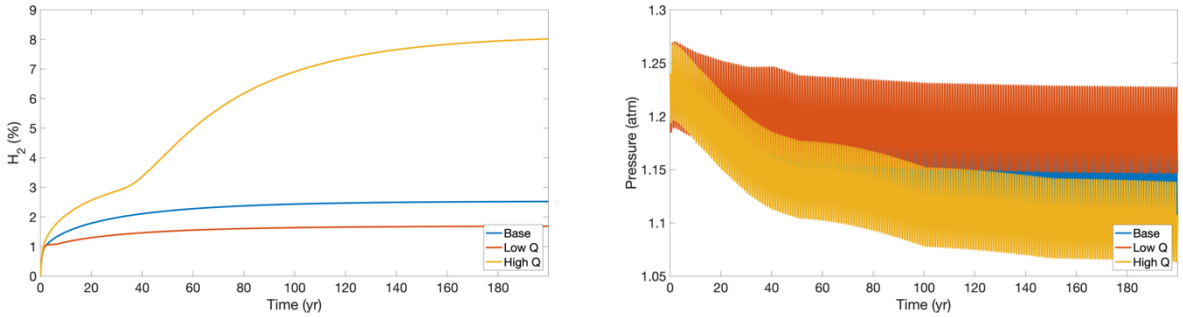

(a) (b)

Figure 11. The (a) hydrogen concentration and (b) canister pressure for the base DOE canister configuration.

A summary of the hydrogen, pressure and oxygen concentrations across the modeled cases is shown in Table 4. The densely packed 18-inch case shows the highest hydrogen concentrations due to its highest surface area to volume ratio.

Table 4. Summary of Results.

Case / Variable Max	Pressure (atm)	H_2 (%)	O_2 (%)
Base Configuration (18W)	1.27	2.1	9e-7
Low decay heat (6W)	1.27	1.4	3e-7
High decay heat (42W)	1.28	6.5	2e-6
Densely packed 18-inch (18W)	1.28	4.0	7e-7
Low decay heat (6W)	1.28	2.8	3e-7
High decay heat (42W)	1.28	11.3	2e-6
Densely packed 24-inch (18W)	1.27	2.5	9e-7
Low decay heat (6W)	1.27	1.7	3e-7
High decay heat (42W)	1.27	8.0	3e-6

4. Conclusions

An update to the surface chemistry of the DOE sealed standard canister was made to allow for water radiolysis reactions and a series aluminum oxyhydroxide reactions to occur for a stable O^- group. This results in a cleaner roll-over effect than simply applying a step change to the g-value of the hydrogen generation. The result is that the roll-over effect occurs sooner than previous models, and that this roll-over effect results in a lower total amount of hydrogen formed. For the nominal case with dried fuel, the

hydrogen generation is only about 2%, so it is even less than the flammability limit if it were exposed to oxygen. For the densely packed 18-inch case the total hydrogen concentration is only around 4% with the nominal decay heat. For the densely packed 24-inch case the total hydrogen concentration is only 2.5%, roughly 20% higher than the original packing design, and still under flammability conditions if exposed to oxygen.

REFERENCES

Abashian, M., 1998 Mined Geologic Disposal System Draft Disposability Interface Specification, DI Number B00000000-0 171704600-00108 REV 00. Civilian Radioactive Waste Management System Management & Operating Contractor (draft).

Abboud, A.W. and Huang, H., 2018. Transient Coupled Chemical-Thermal-Fluid Field Simulation of Sealed Aluminum-clad Spent Nuclear Fuel Storage Canister, Tech. rep. INL/EXT-18-51683.

Abboud, A.W. and Huang, H., 2019. Sensitivity Study of Coupled Chemical-CFD Simulations for Sealed and Unsealed Aluminum-clad Spent Nuclear Fuel Storage Canisters. Idaho National Laboratory, Tech. rep. INL/EXT-19-52650.

Abboud, A.W., 2021. Modeling Summary of ASNF in DOE Sealed Standard Canisters, Idaho National Laboratory, Tech. rep. INL/EXT-21-64413.

Abboud, A.W., 2022. Extended Modeling of DOE Sealed Canisters with Updated Chemistry Models. Idaho National Laboratory, Tech. rep. INL/RPT-22-67694.

Abboud, A. W. 2022b. Sensitivity study of coupled chemical-CFD simulations for analyzing aluminum-clad spent nuclear fuel storage in sealed canisters. Nuclear Engineering and Design, 390, 111691.

Abboud, A.W., 2023. Chemical Model of Pressure Bounding Conditions in a DOE Standard Canister. Idaho National Laboratory, Tech. rep. INL/RPT-23-70934.

Abboud, A.W., 2023b. Coupled chemical–CFD modeling of unsealed dry storage of advanced test reactor spent fuel. Annals of Nuclear Energy, 183, p.109646.

Arkhipov, O.P., Verkhovskaya, A.O., Kabakchi, S.A., and Ermakov, A.N., 2007. Development and verification of a mathematical model of the radiolysis of water vapor. Atomic Energy, 103(5):870.

Atkinson, R., Baulch, D.L., Cox, R.A., Crowley, J.N., Hampson, R.F., Hynes, R.G., Jenkin, M.E., Rossie, M.J., and Troe, J., 2004. Evaluated kinetic and photochemical data for atmospheric chemistry: volume I – gas phase reactions of X, HOx, NO2, and SOx species. Atmospheric Chemistry and Physics, 4(6): 1461-1738.

Bulearca, A.M., Mihaela, A. Calinescu, I., and Lavric, V., 2010. Model Studies of NOx and SOx reactions in Flue gas treatment by electron beam. UPB Sci Bull, Series B, 72(1):101-112.

Buxton, G. V.; Greenstock, C. L.; Helman, W. P.; Ross, A. B., Critical review of rate constants for reactions of hydrated electrons, hydrogen atoms and hydroxyl radicals (·OH/·O-) in aqueous solution. J. Phys. Chem. Ref. Data 1988, 17 (2), 513-886.

Conrad, J. K.; Pu, X. F.; Khanolkar, A.; Copeland-Johnson, T. M.; Pilgrim, C. D.; Wilbanks, J. R.; Parker-Quaife, E. H.; Horne, G. P., Radiolytic Gas Production from Aluminum Coupons (Alloy 1100 and 6061) in Helium Environments-Assessing the Extended Storage of Aluminum Clad Spent Nuclear Fuel. *Materials* **2022,** *15* (20), 7317.

Conrad, J.K., and Horne, G.P. 2023. The Fate of Oxygen Radical Species in Corroded Aluminum Alloys under Irradiation. Idaho National Laboratory, Tech rep. INL/RPT-23-71706.

U.S. Department of Energy (DOE), 2008, *Waste Acceptance System Requirements Document*, DOE/RW-0351, Revision 5, ICN 0.1

Goodwin, D.G., Moffat, H.K., and Speth, R.L. *Cantera: An object-oriented software toolkit for chemical kinetics, thermodynamics, and transport processes*. http://www.cantera.org, 2017. Version 2.3.0. doi:10.5281/zenodo.170284

Hilton, B.A. 2000. Review of Oxidation Rates of DOE Spent Nuclear Fuel Part 1: Metallic Fuel. Tech. rep. Argonne National Laboratory, AN-00/24.

Horne, G.P., Conrad, J.K., Copeland-Johnson, T.M., Pu, X., Khanolkar, A., Wilbanks, J.R. and Pilgrim, C.D. 2022. Milestone 1.2.10: Steady-state H2 roll-over point data for aluminum alloys 1100 and 6061. INL-RPT-22-68379. Tech. Rep. Idaho National Laboratory.

Illum, D.B., 1996. ATR Fuel Summary Report. Tech. Report INEL-96/300.

Incropera F.P., DeWitt, D.P., Bergman, T.L. and Lavine, A.S., 2007. Fundamentals of Heat and Mass Transfer, Sixth Edition, John Wiley and Sons, Hoboken, NJ.

Kaddissy, J. A.; Esnouf, S.; Durand, D.; Saffre, D.; Foy, E.; Renault, J.-P., Radiolytic Events in Nanostructured Aluminum Hydroxides. J. Phys. Chem. C 2017, 121, 6365-6373.

Kaddissy, J. A.; Esnouf, S.; Saffre, D.; Renault, J.-P., Efficient hydrogen production from irradiated aluminum hydroxides. International Journal of Hydrogen Energy 2019, 44, 3737-3743.

Lacroix L., Maxted G., Hartman W., Fair H., Sindelar R., Bates W., Dunmuir M., Moore E., Changler M., Rose D., Connolly M., Birk S., Smith K., Luke D. 2017. Aluminum Clad Spent Nuclear Fuel: Technical Considerations and Challenges for Extended (50 years) Dry Storage: Tech. Rep., U.S. Department of Energy/ID RPT-1575.

Le Caer, S., Water Radiolysis: Influence of Oxide Surfaces on H2 Production under Ionizing Radiation. Water 2011, (3), 235-253.

Lister, T. 2018. Vapor Phase Corrosion Testing of Pretreated AA1100. Tech. Rep. Idaho National Laboratory, INL/EXT-18-52249.

Lister, T and Orme, C. 2019. Analysis of Vapor Phase Corrosion of Pretreated Aluminum Alloys. Tech. Rep. Idaho National Laboratory, INL/EXT-19-55558.

Lundberg, L.B., 1994. Corrosion of Spent ATR Fuel Elements Relative to Their Dry Storage. Tech. Rep. EG&G Idaho, Inc. ERA-NRE-94-096.

Milosavljevic, B. H.; Thomas, J. K., Reactions of Electrons on the Surface of γ-Al2O3. A Pulse Radiolytic Study with 0.4 MeV Electrons. J. Phys. Chem. B 2003, (107), 11907-11910.

Morton, D.K., 1999, Preliminary Design Specification for Department of Energy Standardized Spent Nuclear Fuel Canister, National Spent Nuclear Fuel Program, DOE/SNF/REP-011, Rev. 3, Vol. I and II.

Mortensen, K., 2016, EDF-10891, Decay Heat of ATR Elements to be Transferred from CPP-666 FSA to IFSF, Tech. rep., Idaho National Laboratory.

Olson, L., Verst, C., d'Entremont, A., Fuentes, R., and Sindelar, R. 2019. Characterization of Oxide Films on Aluminum Materials following Reactor Exposure and Wet Storage in the SRS L-Basin. Tech. Rep. Savannah River National Laboratory, SRNL-STI-2019-00058.

Orano, 2019, *Feasibility Evaluation of ATR4 Buckets in DOE Standardized Canisters Fit and Criticality*, RPT-3022527-000.

Parker-Quaife E.H. and Horne, G.P. 2021. Milestone 2.8: Preliminary Radiolytic Gas Generation Measurements from Helium-Backfilled Samples. Tech. Rep. Idaho National Laboratory, INL/EXT-21-61404.

Petersen, G. 2022. Bounding Pressure and Flammability Evaluations for a DOR Standard Canister Loaded with ASNF. Tech. Rep. Idaho National Laboratory, INL/RPT-22-02265.

Polkinghorne, S.T. and Lacy, J.M. 1991. Thermophysical and Mechanical Properties of ATR Core Materials, Report No. PG-T-91-031, EG&G Idaho Inc.

Siemens, 2022. User Guide: Star-CCM+ v17.04.008R8.

Snow, S.D. 2008. Design Considerations for the Standardized DOE SNF Canister Internals, Tech. Rep., U.S. Department of Energy, DOE/SNF/DSN-19.

Snow, S., 2019, Supplemental Evaluation of the DOE Standard SNF Canister for Accidental Drops, ECAR 4632, Revision 08.

Stewart, D. 2012, ECAR-2906. ATR Fuel Element In-Air Dose Rate Estimates Base on Heat Generation, Tech rep., Idaho National Laboratory.

Taylor, L.L. 2004. Packaging Strategies for Criticality Safety for “Other” DOE Fuels in a Repository, Tech. Rep., U.S. Department of Energy, DOE/SNF/REP-090.

Thomas, J. K., Physical Aspects of Radiation-Induced Processes on SiO2, γ-Al2O3, Zeolites, and Clays. Chem. Rev. 2005, 105, 1683-1734.

Verst, C. 2022. Interim Irradiation and Measurement of As-dried, as-corroded and MURR Hydrated Oxide Specimens (Large Coupons). Savannah River National Laboratory, Tech. rep. SRNL-L3110-2022-00001.

Winston, P., Middlemas, S., Winston, A., Aguiar, J., Liu, X., Tolman, K. 2020. Aluminum Spent Fuel Performance in Dry Storage Task 4 Aluminum Oxide Sampling of ATR Dry Stored Fuel, Technical Report, Idaho National Laboratory, INL-EXT-20-58404, 2020.

Wittman, R., Hanson, B. 2015. Radiolysis model analysis for a used fuel storage canister. In proceedings: IHLRWM April 2015.

Westbrook, M.L., Sindelar, R.L., Fisher, D.L. 2015. Radiolytic hydrogen generation from aluminum oxyhydroxide solids: theory and experiment. Journal Radioanalytical and Nuclear Chemistry, 303, pp 81-86.

Wren, J. C., & Ball, J. M. (2001). LIRIC 3.2 an updated model for iodine behaviour in the presence of organic impurities. *Radiation Physics and Chemistry*, *60*(6), 577-596.

Zalupski, P. 2018 Aluminum Clad Spent Nuclear Fuel Task 2: Oxide Layer Radiolytic Gas Generation Resolution Experiment Test Plan. Idaho National Laboratory, INL/EXT-18-45858.

Zabetakis, M.G. 1965. *Flammability characteristics of combustible gases and vapors*, Bureau of Mines, Washington D.C.

Appendix A
Updated Surface Chemistry

The following is a list of the surface chemistry that is used in the updated model. The previous gas phase chemistry remains the same. Due to Cantera's limitations on maintaining a constant number of surface sites in each reaction, a null(S) is used throughout the surface chemistry to maintain the consistency, this has no associated mass or chemical composition.

```
#AlOOH
surface_reaction('ALO2H(S) + null(S) => ALO2H-(S) +
h+(S)',[GS,0.0,0.0],order="ALO2H(S):0.0
null(S):0.0",options=['negative_orders', 'nonreactant_orders'])

surface_reaction('ALO2H-(S) + null(S) => ALO2-(S) +
H(S)',[1.0e5,0.0,0.0],order="ALO2H-(S):1.0
null(S):0.0",options=['negative_orders', 'nonreactant_orders'])

#or AL-OH2 + h+ -> AL OH + H+
   surface_reaction('H2O(S) + h+(S) => OH(S) + H+(S)',[1.0e-
1,0.0,0.0],options=['negative_orders', 'nonreactant_orders'])


#Water Rad G = -4.1 H2O
   GS2 = 4.2476e-7 * 0.018 * d2
surface_reaction('H2O(S) + 1.253 null(S) => 0.634 electron(S) + 0.046 H(S) +
0.110 H2(S) + 0.558 OH(S) + 0.171 H2O2(S) + 0.634 H+(S) + 0.1
H2Ostar(S)',[GS2*100,0.0,0.0],order="H2O(S):1.0 null(S):\
   0.0")


   surface_reaction('H2Ostar(S)  => H2 +
O(S)',[1.0e5,0.0,0.0],order="H2Ostar(S):1.0
null(S):0.0",options=['negative_orders', 'nonreactant_orders'])


# Eqs in form exp(Ea * TF)
# TF = Ea*((1/298.15-1/T))/R
# note exponent property a^m + a^n = a^(m+n), use backwards
# exp(Ea * TF) = exp(Ea/298.15/R - Ea/T/R) = exp(Ea/298.15/R)*exp(-Ea/R/T)
# then arrehinus A = tabulated A * exp(Ea/298.15/R); R=8314
#tabulated Ea = J/mol, mult x 1e6 to get to J/kmol
#correction factor units in volume of kmol/m^3
#mult by oxide thickness
   c = 15e-6
```

```
#values from Wren, 2000 (LIRIC)
#7
div = (1/298.15-1/300.00)/8.314*2.2e7*26000 #larger at larger T, decs rate
surface_reaction('electron(S) + H2O(S) => H(S) + OH-
(S)',[19*1966.98/div*c,0.0,18.8e6],options=['negative_orders',
'nonreactant_orders'])

#8
surface_reaction('2 electron(S) + 2 H2O(S) => H2(S) + 2 OH-(S) +
null(S)',[5.5e9*3602.5*c,0.0,20.3e6],order="electron(S):2.0
H2O(S):0.0",options=['negative_orders', 'nonreactant_orders'])

#9
surface_reaction('electron(S) + H(S) + H2O(S)=> H2(S) + OH-(S) +
null(S)',[2.5e10*424.65*c,0.0,15.0e6],order="electron(S):1.0 H(S):1.0
H2O(S):0.0",options=['negative_orders', 'nonreactant_orders'\
])

#10
surface_reaction('electron(S) + H+(S) => H(S) +
null(S)',[2.3e11*131.81*c,0.0,12.1e6],options=['negative_orders',
'nonreactant_orders'])

#11
   surface_reaction('OH(S) + electron(S) => OH-(S) +
null(S)',[3.0e10*24.22*c,0.0,7.9e6],options=['negative_orders',
'nonreactant_orders'])


#12
surface_reaction('electron(S) + O2(S) => O2-(S) +
null(S)',[1.8e10*283.68*c,0.0,14.0e6],options=['negative_orders',
'nonreactant_orders'])

#13
surface_reaction('electron(S) + H2O2(S) => OH(S) + OH-
(S)',[1.4e10*491.03*c,0.0,15.36e6],options=['negative_orders',
'nonreactant_orders'])

#14 #type 1360 or 13600 (like others) ?
surface_reaction('electron(S) + O2-(S) + H2O(S) => HO2-(S) + OH-(S) +
null(S)',[1.3e10*241.41*c,0.0,13.6e6],order="electron(S):1.0 O2-(S):1.0
H2O(S):0.0",options=['negative_orders', 'nonreactant_\
orders'])

#15
```

```
surface_reaction('electron(S) + HO2-(S) => O-(S) + OH-
(S)',[3.5e9*499.01*c,0.0,15.4e6],options=['negative_orders',
'nonreactant_orders'])

#16
surface_reaction('electron(S) + O-(S) + H2O(S) => OH-(S) + OH-(S) +
null(S)',[2.2e10*24.22*c,0.0,7.9e6],order="electron(S):1.0 O-(S):1.0
H2O(S):0.0",options=['negative_orders', 'nonreactant_order\
s'])

#17
surface_reaction('H(S) + OH(S) => H2O(S) +
null(S)',[7.0e9*23.26*c,0.0,7.8e6],options=['negative_orders',
'nonreactant_orders'])

#18
   surface_reaction('H(S) + H(S) => H2 + 2
null(S)',[7.75e9*433.3*c,0.0,15.05e6],options=['negative_orders',
'nonreactant_orders'])


#19
surface_reaction('H(S) + O2(S) => HO2(S) +
null(S)',[2.1e10*161.27*c,0.0,12.6e6],options=['negative_orders',
'nonreactant_orders'])

#20
surface_reaction('H(S) + HO2(S) => H2O2(S) +
null(S)',[1.0e10*71.97*c,0.0,10.6e6],options=['negative_orders',
'nonreactant_orders'])

#21
surface_reaction('H(S) + H2O2(S) => OH(S) +
H2O(S)',[9.0e7*620.47*c,0.0,15.94e6],options=['negative_orders',
'nonreactant_orders'])

#22
surface_reaction('H(S) + O2-(S) => HO2-(S) +
null(S)',[2.0e10*71.97*c,0.0,10.6e6],options=['negative_orders',
'nonreactant_orders'])

#23
surface_reaction('OH(S) + O2-(S) => O2(S) + OH-
(S)',[8.0e9*79.61*c,0.0,10.85e6],options=['negative_orders',
'nonreactant_orders'])

#24
```

```
surface_reaction('OH(S) + OH(S) => H2O2(S) +
null(S)',[5.5e9*21.89*c,0.0,7.65e6],options=['negative_orders',
'nonreactant_orders'])

#25
surface_reaction('OH(S) + HO2-(S) => HO2(S) + OH-
(S)',[7.5e9*540.95*c,0.0,15.6e6],options=['negative_orders',
'nonreactant_orders'])

#26
   surface_reaction('OH(S) + H2O2(S) => HO2(S) +
H2O(S)',[2.7e7*545.33*c,0.0,15.62e6],options=['negative_orders',
'nonreactant_orders'])


#27
surface_reaction('OH(S) + H2(S) => H(S) +
H2O(S)',[4.2e7*1513.28*c,0.0,18.15e6],options=['negative_orders',
'nonreactant_orders'])

#28 (check this isnt supposed to be 15.6e6?)
surface_reaction('OH(S) + HO2(S) => O2(S) +
H2O(S)',[6.0e9*9.57*c,0.0,5.6e6],options=['negative_orders',
'nonreactant_orders'])

#29
surface_reaction('O-(S) + OH(S) => HO2-(S) +
null(S)',[2.0e10*22.34*c,0.0,7.7e6],options=['negative_orders',
'nonreactant_orders'])

#30
surface_reaction('H2O2(S) + O-(S) => O2-(S) +
H2O(S)',[2.0e8*540.95*c,0.0,15.6e6],options=['negative_orders',
'nonreactant_orders'])

#31
surface_reaction('H2(S) + O-(S) => H(S) + OH-
(S)',[8.0e7*261.69*c,0.0,13.8e6],options=['negative_orders',
'nonreactant_orders'])

#32
surface_reaction('HO2-(S) + O-(S) => O2-(S) + OH-
(S)',[4.0e8*1966.98*c,0.0,18.8e6],options=['negative_orders',
'nonreactant_orders'])

#33
```

```
surface_reaction('O2(S) + O-(S) => O3-(S) +
null(S)',[3.0e9*91.77*c,0.0,11.2e6],options=['negative_orders',
'nonreactant_orders'])

#34
   surface_reaction('O3-(S) + null(S) => O-(S) +
O2(S)',[3.0e2*101563838.28*c,0.0,45.7e6],options=['negative_orders',
'nonreactant_orders'])


#35
surface_reaction('O3-(S) + H2O2(S) + null(S) => O2-(S) + O2(S) +
H2O(S)',[1.6e6*1966.98*c,0.0,18.8e6],order="O3-(S):1.0 H2O2(S):1.0
null(S):0.0",options=['negative_orders', 'nonreactant_orders'])

#36
surface_reaction('O3-(S) + HO2-(S) + null(S) => O2-(S) + O2(S) + OH-
(S)',[8.9e5*1966.98*c,0.0,18.8e6],order="O3-(S):1.0 HO2-(S):1.0
null(S):0.0",options=['negative_orders', 'nonreactant_orders'])

#37
surface_reaction('O3-(S) + H2(S) + null(S) => O2(S) + H(S) + OH-
(S)',[2.5e5*1966.98*c,0.0,18.8e6],order="O3-(S):1.0 H2(S):1.0
null(S):0.0",options=['negative_orders', 'nonreactant_orders'])

#38
surface_reaction('HO2(S) + O2-(S) => O2(S) + HO2-
(S)',[8.9e7*1966.98*c,0.0,18.8e6],options=['negative_orders',
'nonreactant_orders'])

#39
surface_reaction('HO2(S) + HO2(S) => O2(S) +
H2O2(S)',[2.0e6*1966.98*c,0.0,18.8e6],options=['negative_orders',
'nonreactant_orders'])

#40
surface_reaction('H2O2(S) + null(S) => H+(S) + HO2-
(S)',[0.0356*1966.98*c,0.0,18.8e6],order="H2O2(S):1.0
null(S):0.0",options=['negative_orders', 'nonreactant_orders'])

#41
   surface_reaction('H+(S) + HO2-(S) => H2O2(S) +
null(S)',[2.0e10*c,0.0,0.0],options=['negative_orders',
'nonreactant_orders'])


#42
```

```
surface_reaction('HO2(S) + null(S) => H+(S) + O2-
(S)',[8.0e5*1966.98*c,0.0,18.8e6],order="HO2(S):1.0
null(S):0.0",options=['negative_orders', 'nonreactant_orders'])

#43 #no EA in Wren
surface_reaction('H+(S) + O2-(S) => HO2(S) +
null(S)',[4.5e10*c,0.0,0.0],options=['negative_orders',
'nonreactant_orders'])

#44
surface_reaction('OH(S) + OH-(S) => O-(S) +
H2O(S)',[1.2e10*1966.98*c,0.0,18.8e6],options=['negative_orders',
'nonreactant_orders'])

#45
surface_reaction('O-(S) + H2O(S) => OH(S) + OH-
(S)',[1.7e6*1966.98*c,0.0,18.8e6],options=['negative_orders',
'nonreactant_orders'])

#46f dissociation of water
TCE = 25
T = 300
DW = 1.00017 - 2.36583e-5*TCE - 4.77122e-6*TCE**2 + 8.27411e-9 *TCE**3
#KW = 10**( -4.098 - 3245.5/T + 2.2362e5/T**2 - 3.984e6/T**3 + (13.957 -
1262.3/T + 8.5641/T**2)*np.log(DW) )
KW = 1.0e-14
surface_reaction('H2O(S) + null(S) => H+(S) + OH-
(S)',[1.43e11*KW*c,0.0,0.0],order="H2O(S):1.0
null(S):0.0",options=['negative_orders', 'nonreactant_orders'])

#46b
   surface_reaction('H+(S) + OH-(S) => H2O(S) +
null(S)',[1.43e11*c,0.0,0.0],options=['negative_orders',
'nonreactant_orders'])


   surface_reaction('H2(S) => H2 + null(S)',[1.0e15,0.0,0.0])
```